Met. Mater. Int., Vol. 21, No. 5 (2015), pp. 832~841
doi: 10.1007/s12540-015-5093-3

Hot Tensile Deformation Behavior of Twin Roll Casted 7075 Aluminum Alloy

Lei Wang[1,2], Huashun Yu[1], Yunsoo Lee[2], and Hyoung-Wook Kim[2,*]

[1]Key Laboratory for Liquid-Solid Structural Evolution and Processing of Materials (Ministry of Education), School of Materials Science and Engineering, Shandong University, Jinan 250061, China
[2]Metallic Materials Division, Korea Institute of Materials Science, Changwon, 642-831, Republic of Korea

(received date: 13 February 2015 / accepted date: 18 June 2015)

High temperature deformation behavior of the 7075 aluminum alloy sheets fabricated by twin roll casting and rolling was investigated by hot tensile tests at different temperatures from 350 to 500 °C and various initial strain rates from 1×10^{-3} to 1×10^{-2} s^{-1}. The results show that flow stress increased with increasing initial strain rate and decreasing deformation temperature. A large elongation of 200% was obtained at relatively high strain rate of 5×10^{-3} s^{-1} at 450 °C. It is closely related with the grain boundary sliding at elevated temperature attributed to the recrystallized fine grains and the large volume fraction of high-angle grain boundaries. The fracture transformation mechanism changes from ductile transgranular fracture to ductile intergranular fracture due to the recrystallized fine grains at high temperature. High density and uniform cavities observed in large elongation samples at high temperature reveals the contribution of grain boundary sliding. Necking-controlled failure mode was characterized by rare cavities with low elongation.

Keywords: alloys, twin roll casting, recrystallization, tensile test, elongation

1. INTRODUCTION

The 7××× series alloys, based on the Al-Zn-Mg system, have a combination of high strength and fracture toughness, as well as resistance to stress corrosion cracking [1-3]. 7××× series alloys such as 7075 are often used in transport applications, including marine, automotive and aviation, due to their high strength-to-density ratio. Increased strength of these alloys was anticipated by increasing Zn, Mg, and Cu concentration, as these are the principal basis of precipitation strengthening [4].

Compared to conventional processes such as direct chill casting (DC), twin roll casting (TRC) is more cost-efficient to produce aluminum alloy strip because the strip is directly fabricated from molten metal [5,6]. Moreover, high cooling rate can be obtained because of the direct contact with water-cooled roller. Thus, fine microstructure and small second phase particles induced by high cooling rate could be acquired. By utilization of conventional direct chill casting aluminum alloy, grain size under 10 μm can be obtained by complicated thermal-mechanical treatment, while ultra-fine grained structure can be acquired by simply direct TRC and cold rolling process. Moreover, fine grains and second phase particles induced by high cooling rate are also supposed to have positive effects on deformation behavior [6].

*Corresponding author: hwkim@kims.re.kr

Yun *et al*. [7] produced aluminum sheet using TRC process and discussed the effects of the process in details on the microstructural features. High strength Al-Zn-Mg-Cu alloy sheet by TRC with proper thermo-mechanical processes and grain size was refined to about 10 μm, as reported by Lee *et al*. [8]. And the effect of microstructure on mechanical properties of the strip at ambient temperature was discussed as well.

Usually, 7075 aluminum alloy shows high strength but poor workability. However, fine grains seem as an approach to enhance the formability at elevated temperature. Therefore, the investigation of deformation behavior of the alloys during hot deformation is vital to fully understand their hot workability. Previous studies reported that flow stress of Al-Zn-Mg-Cu aluminum alloys deformed at elevated temperature exhibited a peak stress at a critical strain, and then decreased to fracture showing a dynamic flow softening [9]. Cerri *et al*. [10] carried out a comparative study on the hot workability of 7012 and 7075 alloys under different pretreatments, demonstrating that the peak flow stress of Al-Zn-Mg-Cu alloys was related to the strain rate by the hyperbolic sine equation. And the activation energies for 7012 and 7075 alloy were 141-162 kJ/mol and 143-156 kJ/mol, respectively. Although some experiments have been carried out to investigate the deformation behavior of the aluminum alloys so far, limited datasets are available for studying the hot tensile deformation behavior of 7075 aluminum alloy produced by TRC process. In addi-

tion, conventional studies of hot tensile deformation behavior of aluminum alloy are mostly focused on relatively low strain rates associated with superplastic deformation which are generally of the order of 10^{-4} or 10^{-3} s^{-1} [11,12]. However, this low strain rate cannot meet the demands for components forming in the automotive industry, restraining the commercial applications to limited quantities production. To commercialize the forming process, high strain rate workability is highly needed to be investigated.

In this paper, in order to study the high strain rate workability of the alloys, the hot deformation behavior and the microstructural evolution of 7075 aluminum alloy were investigated systematically.

2. EXPERIMENTAL PROCEDURE

The chemical composition of the studied 7075 aluminum alloy in this research was Al-5.2Zn-2.3Mg-1.5Cu (wt%), as shown in Table 1.

The alloy strip with 4.5 mm in thickness was successfully fabricated by a horizontal type twin roll caster with water-cooled Cu-Cr rolls. The molten alloy heated up to 680 °C was transferred into the preheated tundish and nozzle. The casting roll speed was 5-6 rpm and the roll gap was 4 mm, detailed information can be found in previous reference [8]. Then the casting strip was annealed at 400 °C for 1h and warm rolled at 250 °C to the thickness of 2.0 mm. After re-annealed at same condition, samples were finally cold rolled to a final thickness of 1 mm.

Flat tensile samples with a gauge length of 10 mm and cross section of 5 mm × 1 mm were machined from the rolled sheets parallel to rolling direction (RD). Tensile test were carried out at temperatures and initial strain rates ranging from 350 to 500 °C and 10^{-3} to 10^{-2} s^{-1}, respectively. The samples were hold at desired temperature for 10 minutes before the tensile test in order to homogenize the distribution of temperature.

Samples for optical microscopy (OM) were polished and electrolytic etched for 120 seconds in 5% fluoroboric acid (HBF_4). The microstructure observation was conducted by optical microscope under a polarized light (ECLIPSE MA200). High temperature tensile tests were conducted by a tensile test machine with a three-zone furnace operating at a constant crosshead speed. Fracture surfaces were examined by scanning electron microscopy (SEM, JSM-6610LV). Electron back-scattered diffraction (EBSD) analysis was conducted under a field emission scanning electron microscope (FE-SEM, JSM-7001F). A surface area of approximate 0.4 × 0.3 mm^2 with a scanning step size of 0.2 μm was selected for the measurement of grain size. The diameter of a particular grain using TSL OIM analysis software was calculated by determining the area of a grain. The boundaries of grains or subgrains were defined as low angle boundaries, medium angle boundaries and high angle boundaries with misorientation angles of 1-5°, 5-15° and greater than 15°, respectively. EBSD line scanning was carried out to measure the boundaries misorientation angle.

3. RESULTS

3.1. Initial microstructure

As shown in Fig. 1(a), the relatively fine and equiaxed grains were observed in the as-cast TRC alloy strip. However, close observation shows that the grain size was slightly different from the surface to center. The grain size was measured by linear intercept method. Slightly smaller grain size in the vicinity of the surface (~39 μm) was observed in Fig. 1(b), while it was about 41 μm at center area (see Fig. 1(c)). Moreover, the secondary dendrite arm spacing at surface area (2-4 μm) was measured smaller than that of center area (5-7 μm). High cooling rate at the sample surface induced by direct contact with water-cooled rollers was considered to increase dendrite nucleation rate and shorten solidification time, thus, resulting in small grain size and fine secondary dendrite arm spacing [13]. The slight microstructural difference was related with the temperature gradient during TRC process [8]. High cooling rate caused by direct contact with the rollers induced finer grains near the surface. However, the grains were elongated along rolling direction without obvious grain boundaries in the final cold-rolled strip, as shown in Fig. 1(d).

Figure 1(e) shows the morphology and distribution of second phase particles in analyzed samples. The small size particles in high number density were probably due to high solidification and cooling rate in TRC process. Compared to conventional casting processes, the fine-grained microstructure and small second-phase particles induced by TRC process is considered to have significant effects on the high temperature deformation properties [6,14].

3.2. Tensile properties at elevated temperature

As shown in Fig. 2, it is revealed that the flow stress regularly decreased with increasing testing temperature and decreasing strain rate. As the deformation temperature increased, dislocations activity was increased, leading to flow stress decreasing. Moreover, dynamic recovery and dynamic recrystallization is considered as the main softening mechanism at high deformation temperature [9-12]. With the strain rate increasing, the enhanced deformation storage energy and the work hardening effect raised the flow stress. It is shown from the curves that the flow stress firstly increased because of the initial strain

Table 1. Chemical composition of the alloys studied (wt%)

Alloy	Zn	Mg	Cu	Mn	Cr	Fe	Si	Ti	Al
7075	5.18	2.27	1.49	0.045	0.22	0.23	0.11	0.050	Bal.

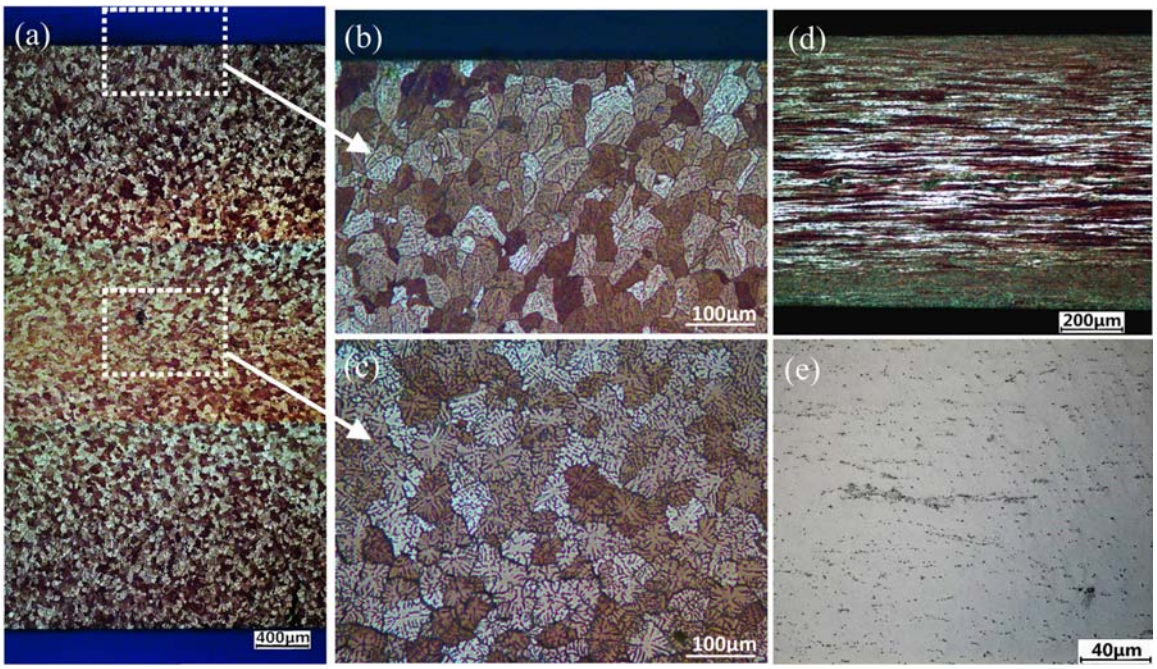

Fig. 1. Microstructure of (a) as TRC-cast 7075 aluminum alloy strip, (b) surface area of (a), (c) center area of (a), (d) final cold rolled strip, and (e) second-phase particles.

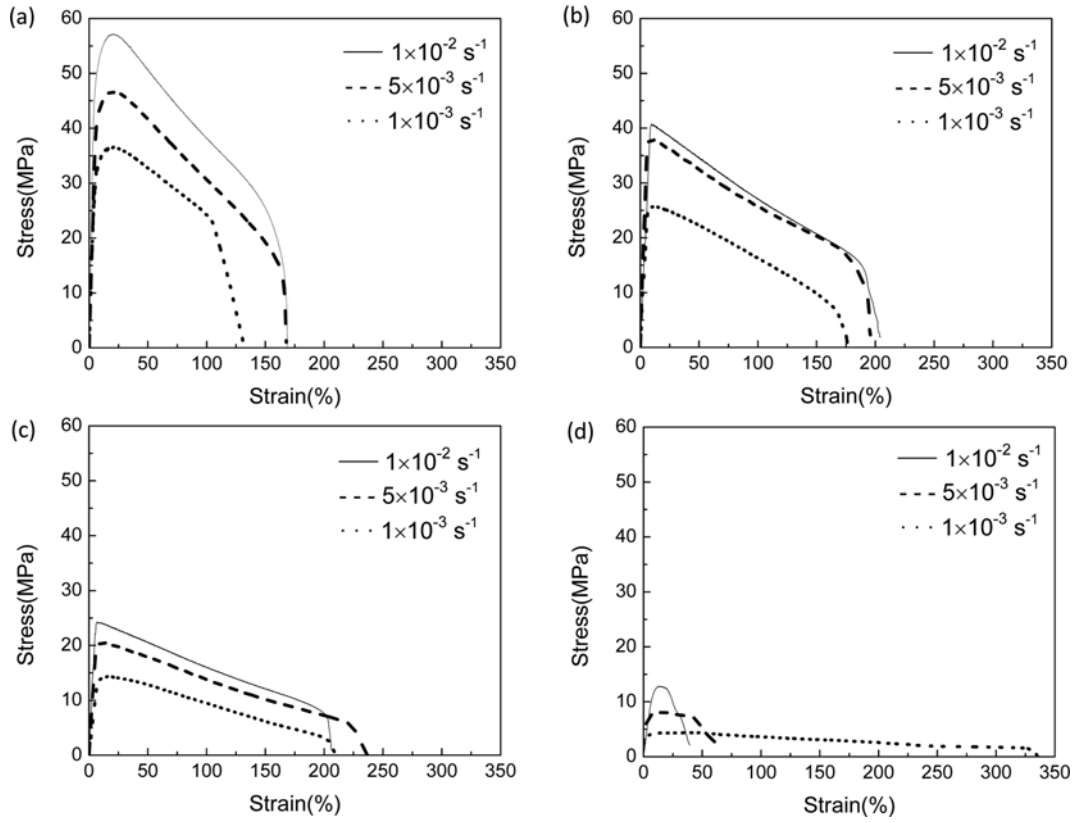

Fig. 2. Nominal stress-strain curves of the cold-rolled AA7075 alloy tested at temperature of (a) 350 ℃, (b) 400 ℃, (c) 450 ℃, and (d) 500 ℃.

hardening and gradually decreased with increasing strain, followed by a dramatic decrease, finally to fracture. The tendency of tensile curves didn't vary significantly from 350 to 450 ℃ when tested at various strain rate (see Fig. 2(a), (b),

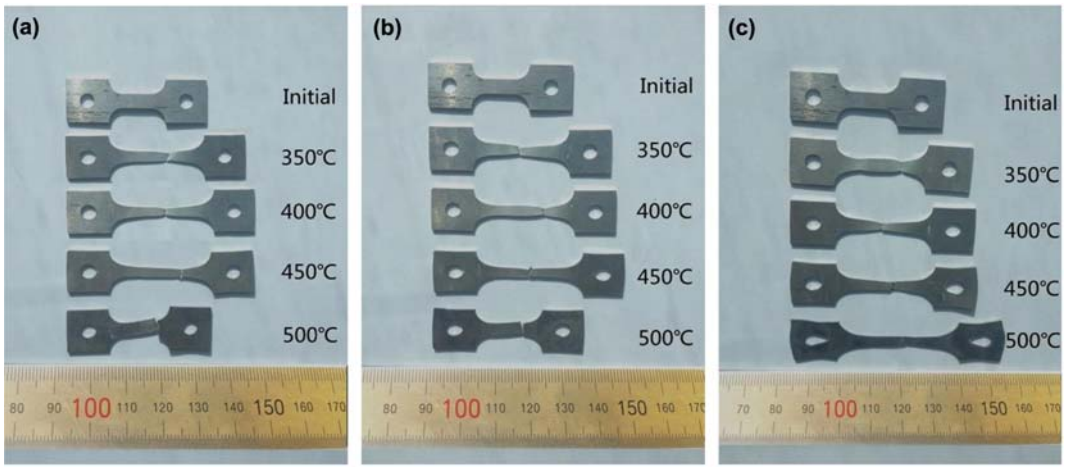

Fig. 3. Appearance of the tensile tested samples at various conditions. (a) $\dot{\varepsilon}$ = 0.01/s, (b) $\dot{\varepsilon}$ = 0.005/s, and (c) $\dot{\varepsilon}$ = 0.001/s.

and (c)). However, in case of high temperature and low strain rate, the curve seemed to reach a steady-equilibrium state (Fig. 2(d)), revealing a homogenous deformation without obvious necking during the test. It is worth noting that, relatively large elongation was obtained at high strain rates of 5×10^{-3} and 10^{-2} s^{-1} as shown in Fig. 2(b) and (c).

Figure 3 shows the tensile samples deformed to fracture at different conditions and the initial sample was compared. It is revealed that the elongation of the 7075 aluminum alloy tested at temperatures of 350, 400 and 450 ℃ was insensitive to both the strain rates and deformation temperatures, compared to that deformed at 500 ℃.

Figure 4 presents the variation in elongation to failure with deformation temperatures and strain rates. The elongation appeared to increase with the increase of testing temperature from 350 to 450 ℃ in all cases of strain rate, but it showed a big decrease at 500 ℃ except the condition of 1×10^{-3} s^{-1}. The highest elongation of 235% was obtained at 500 ℃ under the initial strain rate of 1×10^{-3} s^{-1}. Furthermore, it should be noticed that when the sample deformed at 450 ℃, an elongation peak (~200%) can be observed under relatively high strain rate of 5×10^{-3} s^{-1} in accordance with tensile curves mentioned above (Fig. 2(c)).

3.3. Constitutive equation

From the engineering tensile stress-strain curves shown in Fig. 2, the true peak stresses (σ_p) at the deformation conditions were measured. It is revealed that peak stress decreased with increasing testing temperature and decreasing strain rate. These results were also summarized in Table 2.

Following constitutive equations are found to be most suitable for application in high temperature deformation over a wide range stresses [15].

$$\dot{\varepsilon} = A[\sinh(\alpha\sigma)]^n \exp\left(-\frac{Q}{RT}\right) \tag{1}$$

$$Z = \dot{\varepsilon}\exp\left(\frac{Q}{RT}\right) = A[\sinh(\alpha\sigma)]^n \tag{2}$$

where A, α and n are constants, Q is the deformation activation

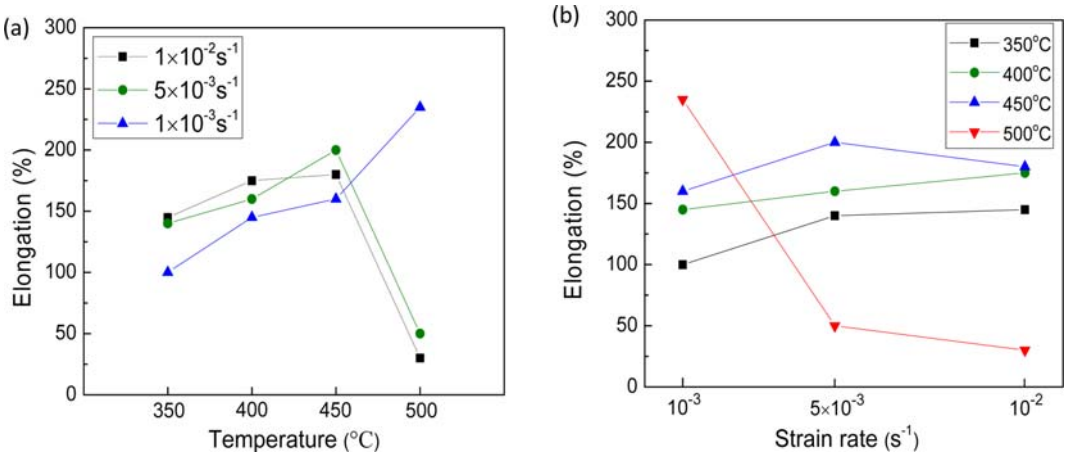

Fig. 4. Elongation to failure as a function of (a) testing temperature and (b) strain rate.

Table 2. Peak stress of 7075 aluminum alloy deformed at various conditions

Strain rate (s^{-1})	Peak stress (MPa)			
	350 ℃	400 ℃	450 ℃	500 ℃
10^{-3}	51.00	34.43	19.29	7.90
5×10^{-3}	65.92	53.01	28.25	10.20
10^{-2}	78.23	54.19	32.12	18.78

energy (kJ/mol), R is the universal gas constant (8.314 J/mol·K), T is the absolute temperature (K) and Z is the Zener-Holloman parameter related to deformation condition.

$$\alpha = \left[\frac{\partial \ln\dot{\varepsilon}}{\partial \sigma}\right]_T \Big/ \left[\frac{\partial \ln\dot{\varepsilon}}{\partial \ln\sigma}\right]_T \approx \beta/n_1 \quad (3)$$

For the present study, the σ value is calculated by using σ_p (MPa) (see Table 2). The α value can be defined by $\alpha \approx \beta/n_1$ [16,17] as shown in Eq. (3), where β and n_1 was evaluated as 0.136 and 4.187 taken as the average values of slopes of the $\ln\dot{\varepsilon}$ vs. σ_p plots and the $\ln\dot{\varepsilon}$ vs. $\ln\sigma_p$ plots (Fig. 5(a) and (b)), respectively. Hence $\alpha = 0.0325$ was determined.

The activation energy (Q) for high temperature deformation is determined by the following equation derived by Eq. (1) [18-21]:

$$Q = R\left[\frac{\partial \ln\dot{\varepsilon}}{\partial \ln[\sinh(\alpha\sigma)]}\right]_T \Big/ \left[\frac{\partial \ln[\sinh(\alpha\sigma)]}{\partial(1/T)}\right]_{\dot{\varepsilon}} \quad (4)$$

where σ_p (MPa) was taken for σ value, and $\left[\frac{\partial \ln\dot{\varepsilon}}{\partial \ln[\sinh(\alpha\sigma_p)]}\right]_T$ and $\left[\frac{\partial \ln[\sinh(\alpha\sigma_p)]}{\partial(1/T)}\right]_{\dot{\varepsilon}}$ were determined as 2.816 and 7.543 by estimating the mean slope of the $\ln\dot{\varepsilon}$ vs. $\ln[\sinh(\alpha\sigma_p)]$ plots and $\ln[\sinh(\alpha\sigma_p)]$ vs. (1000/T) plots (Fig. 5(c) and (d)), respectively. Therefore, the activation energy was calculated as 176.6 kJ/mol for TRC 7075 aluminum alloy.

The activation energy of 176.6 kJ/mol for the TRC 7075 aluminum alloy is lower than that of extruded 7075 aluminum alloy (258.09 kJ/mol) [22], rolled 7050 aluminum alloy (256.6 kJ/mol) [23], solution-treated 7012 aluminum alloy (200-230 kJ/mol) [23] and solution treated and extruded 7075 aluminum alloy (300-400 kJ/mol) [24], whereas it is somewhat higher than that of aged 7150 aluminum alloy (158.8-161.4 kJ/mol) [25] and precipitated and over aged 7012 aluminum alloy (141-162 kJ/mol) [24]. As is well established, the dislocations can be pinned by the solute atoms diffusion in the solid solution alloys [26]. Hence, the high content of the solute atoms (Zn, Mg and Cu) in the matrix would raise the required higher energy for dislocation movement. The dislocation movement pinned by solute atoms is corresponding to microstruc-

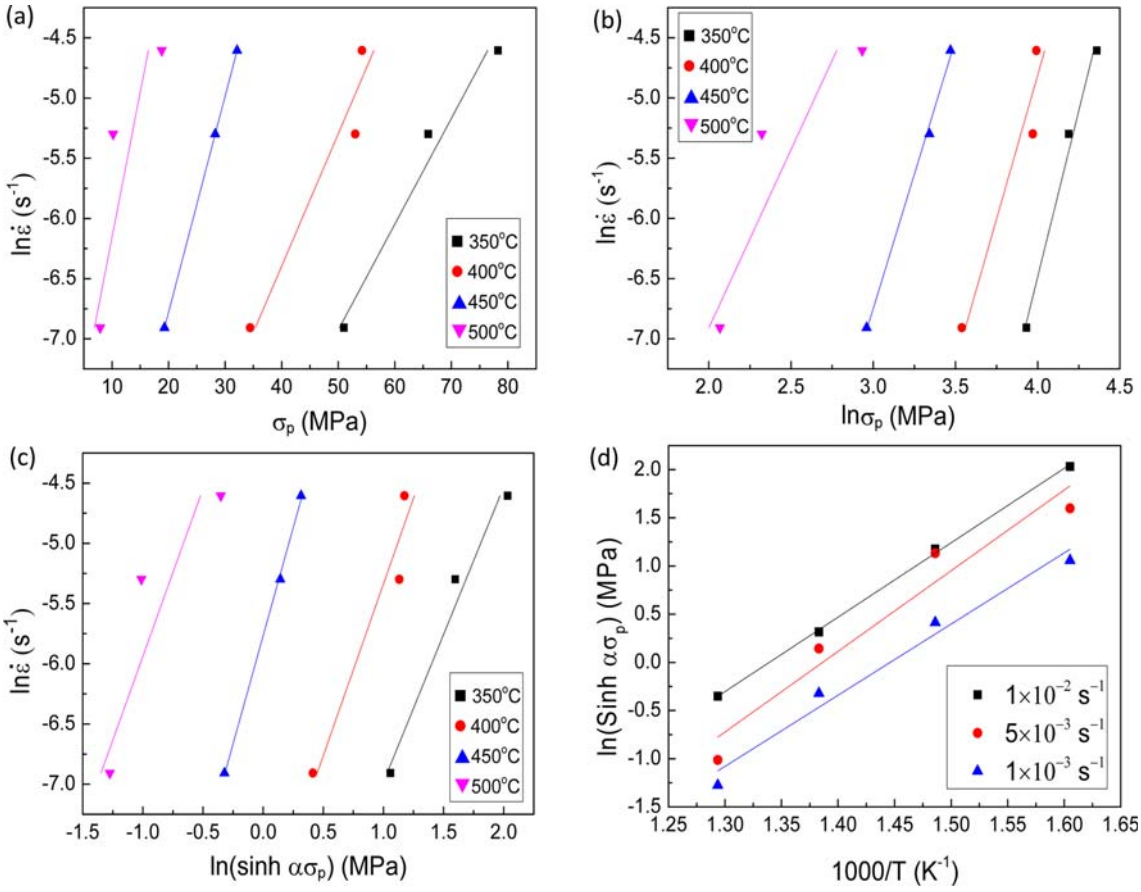

Fig. 5. Plots of (a) $\ln\dot{\varepsilon}$ vs. σ_p, (b) $\ln\dot{\varepsilon}$ vs. $\ln\sigma_p$, (c) $\ln\dot{\varepsilon}$ vs. $\ln(\text{Sinh }\alpha\sigma_p)$, and (d) $\ln(\text{Sinh }\alpha\sigma_p)$ vs. 1000/T.

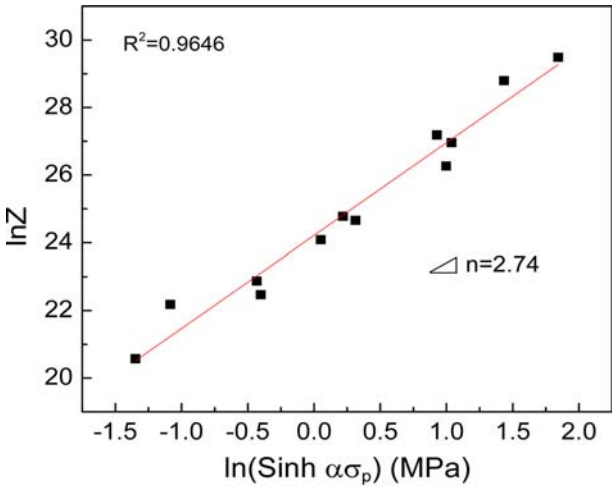

Fig. 6. Plots of lnZ vs. ln(Sinh $\alpha\sigma_p$).

tural difference induced by different alloy fabrication technologies and heat treatment processes [22-25].

Variation relationship of flow stress with deformation temperature and strain rate can be illustrated by the Zener-Hollomon parameter (Z) by Eq. (2). This expression can also be presented as:

$$\ln(Z) = \ln(A) + n\ln[\sinh(\alpha\sigma)] \quad (5)$$

where A and n were determined from the ln(Z) vs. ln[sinh($\alpha\sigma_p$)] plots. The values of n and A were determined as 2.744 and 3.278×10^{10}, respectively. And the expression was represented as:

$$\ln(Z) = 24.213 + 2.744\ln[\sinh(0.0325\sigma_p)] \quad (6)$$

Equation (6) presents the relationship between deformation behavior and deformation conditions. It is obvious that Z increased with increasing strain rate and decreasing deformation temperature, which was similar to the variation of the peak flow stress [15]. As is shown in Fig. 6, ln(Z) and ln[sinh($\alpha\sigma_p$)] indicated a quite good linear relationship.

3.4. Microstructural evolution during deformation

As previously mentioned, the samples were hold at desired temperature for 10 minutes before the tensile loading to get homogenization. Figure 7 gives the microstructure of 7075 alloy specimens which was corresponding to the initial microstructure before tensile loading at the testing temperature. As shown in Fig. 7(a), static recrystallization was hard to occur at 300 °C, while recovery occupied the dominant mechanism. At 400 °C, partial grains appeared to recrystallize and some fine grains appeared along the elongated ones (Fig. 7(b)), while the static recrystallization was completely accomplished at 450 and 500 °C and fine grains were observed through the whole area (Fig. 7(c) and (d)). The difference of initial microstructure is

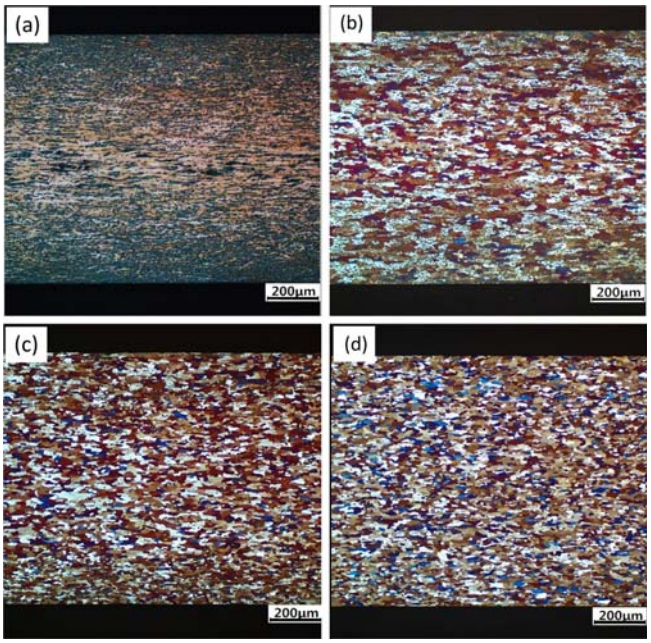

Fig. 7. The initial microstructure before tensile loading at the tested temperatures: (a) 350 °C×10 min, (b) 400 °C×10 min, (c) 450 °C×10 min, and (d) 500 °C×10 min.

considered to make difference to deformation behavior. The possibility of grain boundary sliding (GBS) is available due to fine grains induced by static recrystallization treated at high temperature, which is beneficial to large fracture elongation [27]. These results accorded with the elongation behavior shown in Fig. 4. The elongation to fracture increased with the increasing testing temperatures as a result of the occurrence of fine grains at high temperatures which could contribute to GBS.

Optical microstructures of samples deformed to failure are shown in Fig. 8. At low strain rate of 10^{-3} s^{-1}, the grains were elongated and band-like at 350 °C (Fig. 8(a)). The microstructure deformed at this temperature was recovered without recrystallization. At 400 °C, few fine grains appeared along the elongated one (Fig. 8(b)), while the grains were disintegrated to notably fine and equiaxed in the whole area at 450 and 500 °C (Fig. 8(c) and (d)). It is worth noting that fine grains were also observed throughout the sample thickness at relatively high strain rate of 5×10^{-3} s^{-1} (Fig. 8(e)). These fine grains are closely related with the recrystallization behavior. Reported literature indicates that dynamic recrystallization was generally favored at low Z values which corresponded to low strain rate and high deformation temperature [26]. Fine grains observed in microstructure were considered to be beneficial to large elongation because of the contribution of GBS [27]. Thus, the fracture elongation increased from 350 to 500 °C under the strain rate of 10^{-3} s^{-1} (Fig. 4). In addition, large fracture elongation was also obtained even at a relatively high strain rate of 5×10^{-3} s^{-1} at 450 °C corresponding to its fine

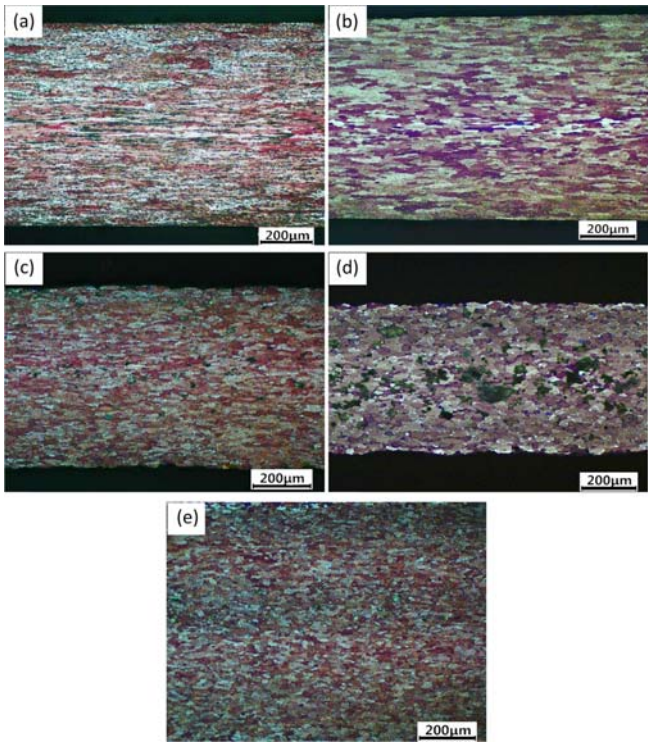

Fig. 8. Microstructure of 7075 aluminum alloy samples deformed to failure at various conditions: (a) 1×10^{-3} s^{-1}, 350 °C; (b) 1×10^{-3} s^{-1}, 400 °C; (c) 1×10^{-3} s^{-1}, 450 °C; (d) 1×10^{-3} s^{-1}, 500 °C; (e) 5×10^{-3} s^{-1}, 450 °C.

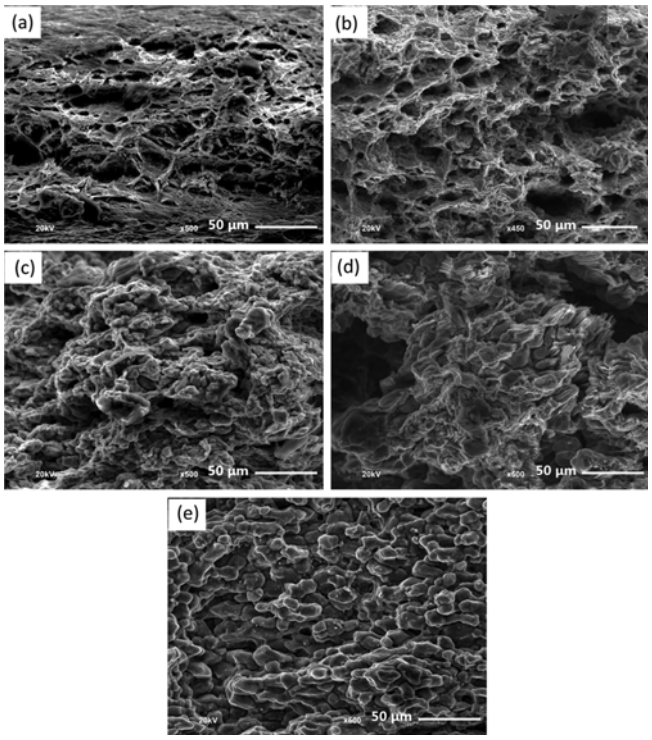

Fig. 9. Fracture surface of the 7075 aluminum alloy deformed at different conditions: (a) 1×10^{-3} s^{-1}, 350 °C; (b) 1×10^{-3} s^{-1}, 400 °C; (c) 1×10^{-3} s^{-1}, 450 °C, (d) 1×10^{-3} s^{-1}, 500 °C; (e) 5×10^{-3} s^{-1}, 450 °C.

microstructure (Fig. 8(e)). Moreover, as shown in Fig. 8(a) and (b), in which deformed at 350 and 400 °C, the different fraction of recrystallization through the thickness was observed. This recrystallization inhomogeneity was attributed to the microstructural non-uniformity of the alloy sheet from surface to center showed in Fig. 1(b) and (c). In addition, the inhomogeneity of particle distribution through the thickness was also observed in the as-cast TRC strip (Fig. 1(e)). Thus, non-uniform particle simulated nucleation was likely to affect the inhomogeneous recrystallization from the sample surface to center [14]. High temperature deformation is considered to improve the microstructural homogeneity throughout the whole samples (Fig. 8(c), (d), and (e)).

Figure 9 shows fracture surface of the 7075 aluminum alloy deformed at different conditions. The fracture surface was typical ductile transgranular mode [28] characterized by dimples with different sizes when the alloy was deformed at 350 and 400 °C under high Z value, as shown in Fig. 9(a) and (b).

The fracture surface of the alloys deformed at 450 and 500 °C under low Z value (Fig. 9(c) and (d)) was typical ductile intergranular mode characterized by relatively smooth surfaces that the topography of grains was clearly observed, revealing the occurrence of grain boundary sliding. Whiskers were also observed on the intergranular fracture surface (Fig. 9(d)). These whiskers were thought to form through viscous flow of a liquid-like grain boundary sliding (GBS) [29]. It should be noted that, clear grain boundaries were found under the condition of 450 °C and 5×10^{-3} s^{-1}, revealing typical ductile intergranular fracture mechanism.

4. DISCUSSION

4.1. Effect of microstructural evolution

Figure 10 presents the orientation imaging maps of samples deformed to fracture at various conditions. These observations are in agreement with optical microstructure as shown in Fig. 8. Large and elongated grains were observed paralleled to the tensile axis when deformed at 350 and 400 °C under 1×10^{-3} s^{-1} (Fig. 10(a) and (b)). It is an evidence that recovery is the dominate mechanism rather than recrystallization [28]. With the increasing deformation temperature to 450 °C and 500 °C (Fig. 10(c) and (d)), more and more fine grains appeared along the elongated grains. And most large band-like grains were replaced by equiaxed and fine grains throughout the whole sample thickness. Recrystallization occurred during tensile deformation resulted in the grain refinement. In addition, fine grains were also observed at 450 °C under relatively high strain rate of 5×10^{-3} s^{-1}. Previous literature [27] reported that the small size grains were induced by recrystallization and had a positive effect on the ductility of aluminum alloy by the contribution of grain boundary sliding.

As is shown in Fig. 11, the fraction of fine grains (<10 μm)

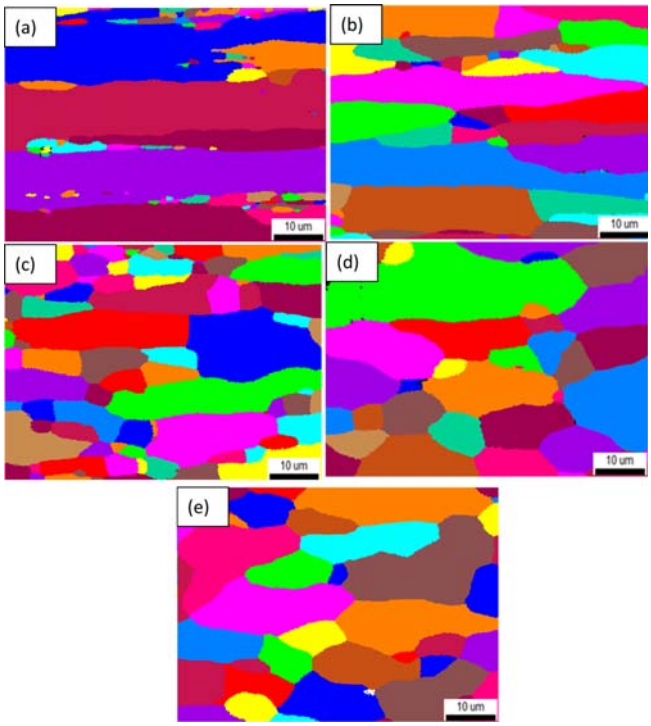

Fig. 10. OIM micrographs of 7075 aluminum alloy samples deformed at: (a) 1×10^{-3} s^{-1}, 350 °C; (b) 1×10^{-3} s^{-1}, 400 °C; (c) 1×10^{-3} s^{-1}, 450 °C, (d) 1×10^{-3} s^{-1}, 500 °C; (e) 5×10^{-3} s^{-1}, 450 °C.

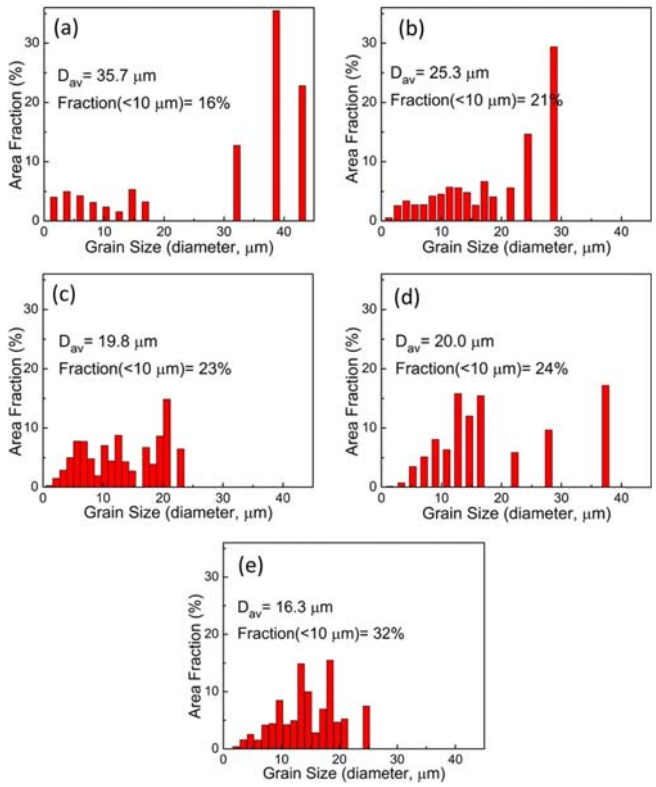

Fig. 11. Grain size distribution of 7075 aluminum alloy samples deformed at: (a) 1×10^{-3} s^{-1}, 350 °C; (b) 1×10^{-3} s^{-1}, 400 °C; (c) 1×10^{-3} s^{-1}, 450 °C, (d) 1×10^{-3} s^{-1}, 500 °C; (e) 5×10^{-3} s^{-1}, 450 °C.

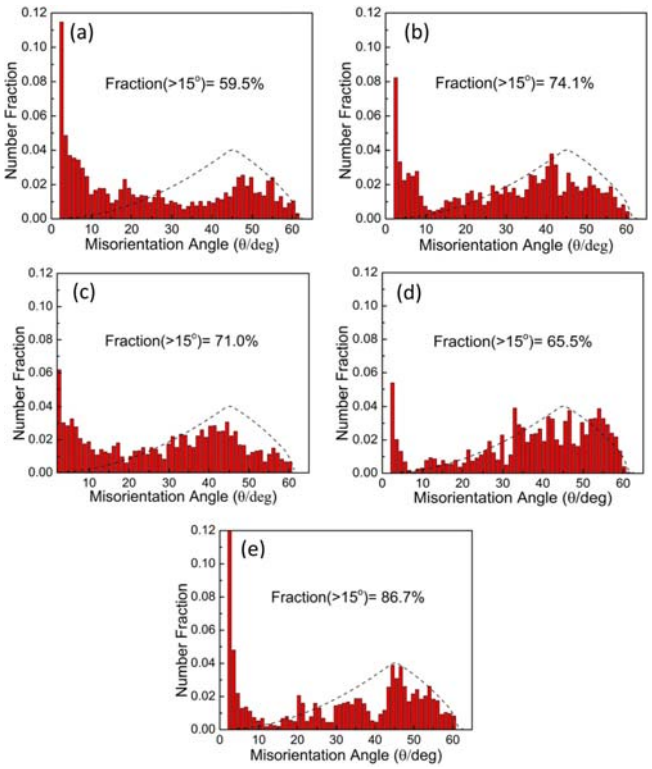

Fig. 12. Misorientation angle of grain boundary of 7075 aluminum alloy deformed at: (a) 1×10^{-3} s^{-1}, 350 °C; (b) 1×10^{-3} s^{-1}, 400 °C; (c) 1×10^{-3} s^{-1}, 450 °C, (d) 1×10^{-3} s^{-1}, 500 °C; (e) 5×10^{-3} s^{-1}, 450 °C.

increased from 16% to 24% and the average grain size decreased from 35.7 μm to 20 μm with the increasing deformation temperatures from 350 °C to 500 °C under strain rate of 1×10^{-3} s^{-1}. Meanwhile, the fine grains accounted for 32% and average grain size was 16.3 μm at 450 °C and 5×10^{-3} s^{-1}. These fine grains were considered to contribute to grain boundary sliding during deformation of the alloys. Thus, these fine grain structures enabled the high contributions of GBS to the total elongation. It is in accordance with the fracture elongation behavior (see Fig. 4) and supported by fracture surface (see Fig. 9(c), (d) and (e)), where intergranular fracture surfaces were observed.

As shown in Fig. 12, the fraction of high angle (>15°) grain boundary (HAGB) increased from 59.5% to 65.5% from 350 °C to 500 °C. Simultaneously, the alloy deformed at 450 °C and 5×10^{-3} s^{-1} showed high fraction of HAGBs of 86.7%. T. Watanabe [30] suggested that the high ratio of HAGBs promoted grain boundary sliding. Therefore, the combination of fine grains and high angle grain boundaries was responsible to large fracture elongation of alloy (shown in Fig. 4) by the contribution of grain boundary sliding.

4.2. Effect of deformation condition

Figure 13 shows the relationship of flow stress to strain rate at various deformation temperatures. The slope of curves is

defined as high strain rate sensitivity (m). It is well known that m>0.33 is a characteristic of superplastic metals and alloys [31]. Generally, high m value is corresponding to high elongation [31]. From Fig. 13, it is shown that the m value of the alloy increased with the testing temperature, indicating high fracture elongation at high temperature shown in Fig. 4. Furthermore, the calculated m value for the alloy at 450 and 500 °C was above 0.22, indicating that dislocation creep and grain boundary sliding affected the alloy ductility greatly [32].

The relationship between elongation of the sample and Z parameter is shown in Fig. 14. An inverse proportional relationship was presented. It is revealed that low Z value, which is corresponding to high deformation temperature and low strain rate, was beneficial to large elongation compared to those with high Z value. Hu [23] studied that the deformation mechanism at high Z values was usually dislocation slipping, while it was grain boundary sliding at low Z values. It was because of the fine and equiaxed grains induced by recrystallization (see Fig. 8 and Fig. 10). Thus, decreasing Z value was available to increase the possibility for large elongation. As discussed above, the samples showed high fracture elongation when deformed at 450 °C under 5×10^{-3} s^{-1} and 500 °C under 1×10^{-3} s^{-1} in Fig. 4, which was corresponding to low Z value.

In addition, the relationship of elongation to lnZ was nearly linear fitting except for two large deviation points as shown in Fig. 14. It means that deformed at high temperature of 500 °C, the elongation was significantly sensitive to high strain rate (1×10^{-2} and 5×10^{-3} s^{-1}). As shown in Fig. 1(e), small particles were induced by TRC process due to its high cooling rate. When deformed at low temperatures, particles did not make great difference due to their small size (~1 μm), while when deformed under high strain rate at high temperature, the particles were considered to make more significant effects. And easy void formation resulting in a crack might be a main reason for the low fracture elongation. The strain incompatibility between the matrix and particles leaded to severe strain concentration which increased the possibility of void formation and drastically diminished the ductility [33].

Figure 15 shows microstructure of the polished 7075 aluminum alloy samples deformed to failure at various test conditions respectively. The tensile axis was horizontal. It is implied that some cavities with very small size were developed to be aligned along the tensile axis at low temperature of 350 °C and high strain rate of 1×10^{-2} s^{-1} (Fig. 15(a)). Furthermore, with increasing temperature to 500 °C (Fig. 15(c)), the relatively large and elongated cavities were observed along the strip center. These conditions were consistent with the necking-controlled failure mode [18]. Partial cavity appearance indicated inhomogeneous deformation and corresponded to low fracture elongation (see Fig. 4). However, when the sample deformed at 450 °C under 5×10^{-3} s^{-1} (Fig. 15(b)) and

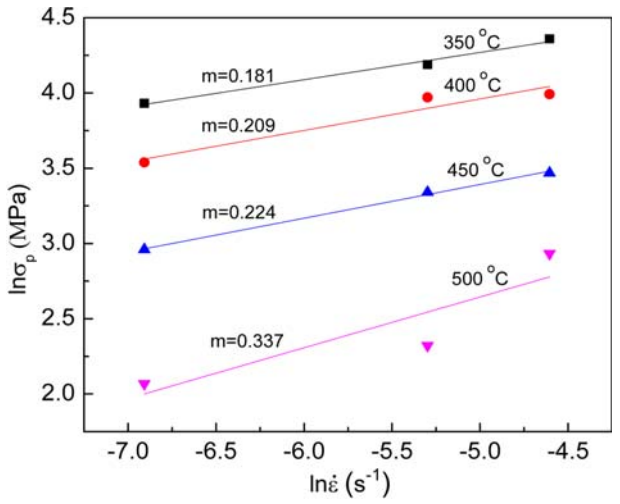

Fig. 13. Logarithmic stress as a function of logarithmic strain rate.

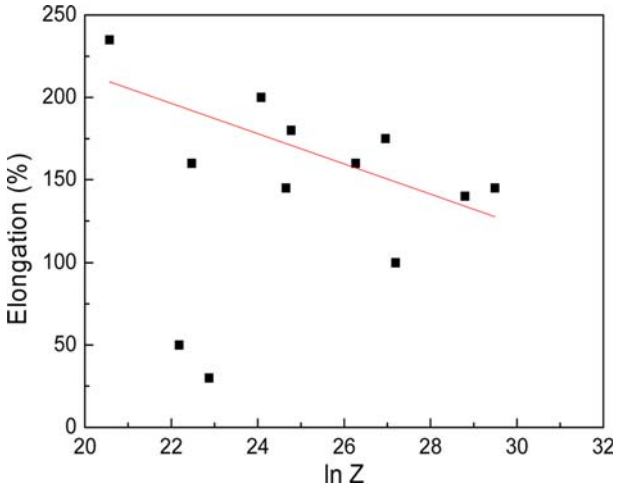

Fig. 14. The relationship of elongation to lnZ.

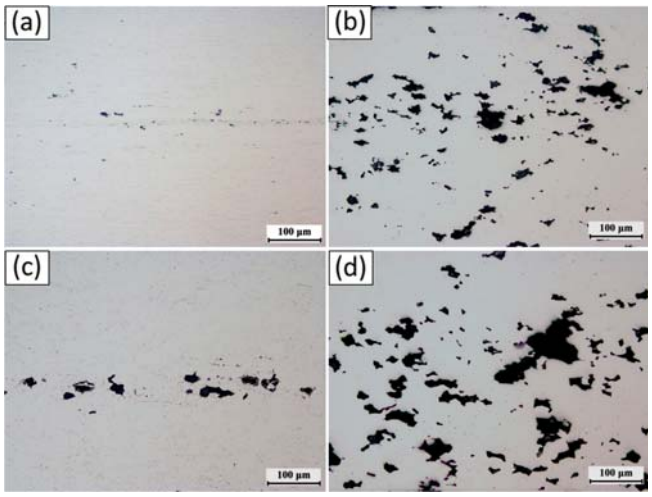

Fig. 15. Microstructure of the polished 7075 aluminum alloy samples deformed to failure at various conditions: (a) 1×10^{-2} s^{-1}, 350 °C; (b) 5×10^{-3} s^{-1}, 450 °C; (c) 1×10^{-2} s^{-1}, 500 °C; (d) 1×10^{-3} s^{-1}, 500 °C.

at 500 °C under 1×10^{-3} s^{-1} (Fig. 15(d)), the cavity population was found to increase remarkable and uniformly distributed. It is evident that the cavity shape was irregular after coalescence. These conditions were a kind of cavitation-controlled failure mode [18]. In this case, interface debonding between adjacent grains is thought to be assisted by grain boundary sliding which is beneficial to large elongation as shown in Fig. 4.

5. CONCLUSIONS

(1) 7075 aluminum alloy was fabricated successfully by TRC process and exhibited large elongation at relatively high strain rate during high temperature deformation. The flow stress which can be presented by a Zener-Holloman parameter in a hyperbolic sine type equation, increased with decreasing temperature from 350 to 500 °C and increased initial strain rate from 1×10^{-3} to 1×10^{-2} s^{-1}. Dynamic fine grains and high fraction of HAGBs were induced by dynamic recrystallization at high temperature.

(2) The elongation of 200% can be obtained under relatively high strain rate of 5×10^{-3} s^{-1}. The combination of fine grains and a sufficient volume fraction of high-angle grain boundaries are responsible to large fracture elongation of alloy by the contribution of grain boundary sliding.

(3) High density and uniform cavities observed in large elongation samples is a kind of the cavitation-controlled failure mechanism, revealing the contribution of grain boundary sliding.

ACKNOWLEDGEMENTS

The authors are grateful for financial support from Korea Institute of Materials Science (KIMS). L. Wang is grateful for financial support from the China Scholarship Council (CSC). Mr. W.K. Kim and Mr. D.A Jo, for strip fabrication and technical assistance, respectively, are also appreciated.

REFERENCES

1. X. Chen, Z. Y. Liu, P. Xia, A. L. Ning, and S. M. Zeng, *Met. Mater. Int.* **19**, 197 (2013).
2. A. Heinz, A. Haszler, C. Keidel, S. Moldenhauer, R. Benedictus, and W.S. Miller, *Mater. Sci. Eng. A* **280**, 102 (2000).
3. J. C. Williams and E. A. Starke Jr., *Acta Mater.* **51**, 5775 (2003).
4. N. P. Jin, H. Zhang, Y. Han, W. X. Wu, and J. H. Chen, *Mater. Charact.* **60**, 530 (2009).
5. J.-H. Cho, H.-W. Kim, C.-Y. Lim, and S.-B. Kang, *Met. Mater. Int*. **20**, 647 (2014).
6. Y.-S. Kim, H.-W. Kwon, J.-W. Park, and D.-J. Kim, *Korean J. Met. Mater.* **51**, 291 (2013).
7. M. Yun, S. Lokyer, and J. D. Hunt, *Mater. Sci. Eng. A* **280**, 116 (2000).
8. Y. S. Lee, W. K. Kim, D. A Jo, C. Y Lim, and H. W. Kim, *Trans. Nonferrous Met. Soc. China* **24**, 2226 (2014).
9. H. Zhang, N. P. Jin, and J. H. Chen, *Trans. Nonferrous Met. Soc. China* **21**, 437 (2011).
10. E. Cerri, E. Evangelista, A. Forcellese, and H. J. McQueen, *Mater. Sci. Eng. A* **197**, 181 (1995).
11. P. Malek. *Mater. Sci. Eng. A* **137**, 21 (1991).
12. D. H. Shin, C. S. Lee, and W. J. Kim, *Acta Mater.* **45**, 5195 (1997).
13. M. S. Turhal and T. Savaskan. *J. Mater. Sci.* **38**, 2639 (2003).
14. K.-S. Kim, S.-Y. Sung, B.-S. Han, C.-Y. Jung, and K.-A. Lee, *Met. Mater. Int*. **20**, 243 (2014).
15. S. Banerjeea, P. S. Robi, A. Srinivasan, and L. P. Kumar, *Mater. Sci. Eng. A* **527**, 2498 (2010).
16. W. J. Liang, Q. L. Pan, Y. B. He, Y. C. Li, and X. G. Zhang, *J. Cent. South Univ. Technol.* **15**, 289 (2008).
17. H. Yu, H. S. Yu, G. H. Min, S. S. Park, B. S. You, and Y. M. Kim. *Met. Mater. Int.* **19**, 651 (2013).
18. R. W. Hertzberg. *Deformation and Fracture Mechanics of Engineering Materials*, fourth ed., p.33, J. Wiley & Sons, Inc. (1996).
19. S. Spigarelli, M. Cabibbo, and E. Evangelista, *J. Bidulska, J. Mater. Sci.* **38**, 81 (2003).
20. F. Bardi, M. Cabibbo, E. Evangelista, S. Spigarelli, and M. Vukcevic, *Mater. Sci. Eng. A* **339**, 43 (2003).
21. E. Cerri, P. Leo, and P. P. De Marco, *J. Mater. Process. Technol.* **189**, 97 (2007).
22. M. R. Rokni and A. Zarei-Hanzaki, *Mater. Des.* **32**, 4955 (2011).
23. H. E. Hu, L. Zhen, L. Yang, W. Z. Shao, and B.Y. Zhang, *Mater. Sci. Eng. A* **488**, 64 (2008).
24. T. Sheppard and A. Jackson, *Mater. Sci. Technol.* **13**, 203 (1997).
25. X. Huang, H. Zhang, Y. Han, and W. Wu, *J. Chen. Mater. Sci. Eng. A* **527**, 485 (2010).
26. W. D. Cao, X. P. Lu, and H. Conrad, *Acta Mater.* **44**, 697 (1996).
27. J. C. Tan and M. J. Tan, *Mater. Sci. Eng. A* **339**, 81 (2003).
28. J. S. Jin, X. Y. Wang, H. E. Hu, and J. C. Xia, *Met. Mater. Int.* **18**, 69 (2012).
29. C. M. Cepeda-Jiménez, O. A. Ruano, M. Carsí, and F. Carreno, *Mater. Sci. Eng. A* **552**, 530 (2012).
30. T. Watanabe, *Mater. Sci. Forum* **375**, 233(1997).
31. T. G. Nieh, J. Wadsworth, and O. D. Sherby, *Superplasticity in Metals and Ceramics*, pp.260-276, Cambridge University Press, Cambridge (1997).
32. O. D. Sherby and J. Wadsworth, *Prog. Mater. Sci.* **33**, 166 (1989).
33. X. Y. Liu, Q. L. Pan, Y. B. He, W. B. Li, W. J. Liang, and Z. M. Yin, *Mater. Sci. Eng. A* **500**, 150 (2009).